INL/JOU-24-77322-Revision-0

The Liquid-Conduction, Vapor-Flow Heat Pipe Model in Sockeye

June 2024

Joshua E Hansel, Carolina da Silva Bourdot Dutra, Lise Cecile Madeleine Charlot, Elia Merzari

INL/JOU-24-77322-Revision-0

The Liquid-Conduction, Vapor-Flow Heat Pipe Model in Sockeye

Joshua E Hansel, Carolina da Silva Bourdot Dutra, Lise Cecile Madeleine Charlot, Elia Merzari

June 2024

Idaho National Laboratory
Idaho Falls, Idaho 83415

http://www.inl.gov

Prepared for the
U.S. Department of Energy
Under DOE Idaho Operations Office
Contract DE-AC07-05ID14517

The Liquid-Conduction, Vapor-Flow Heat Pipe Model in Sockeye

Joshua E. Hansel[a], Carolina da Silva Bourdot Dutra[b], Lise Charlot[a], Elia Merzari[b]

[a]*Idaho National Laboratory, Idaho Falls, ID,*
[b]*The Pennsylvania State University, University Park, PA,*

Abstract

A single-phase heat pipe flow model implemented in the heat pipe application Sockeye is described. This model solves one-dimensional, compressible flow equations for the vapor phase in the center of a heat pipe, which are coupled to the two-dimensional heat conduction equation for the wick, liquid, and cladding, as well as to an ordinary differential equation tracking the working fluid inventory in the evaporator section of the heat pipe. This model is demonstrated with several test problems, including comparisons to analytic solutions for the vapor flow fields, analytic curves for sonic and capillary limitations of heat pipe operation, and some experimental data. The numerical solution gives excellent agreement for verification problems and good agreement with experimental results. Also, demonstrations show that the model is very robust, allowing for full simulations of heat pipe transients, including frozen startup, sonic-limited (supersonic) flow, and heat pipe shutdown.

---

1. Introduction

Heat pipes are highly efficient heat transfer devices that are essentially composed of a small amount of working fluid inside a sealed container with some kind of wicking structure. Heat is applied to the heat pipe, causing the working fluid to evaporate and travel to cooler length(s) of the heat pipe, where the fluid condenses and releases its latent heat. The wicking structure draws the condensed working fluid back to the evaporating section(s), where the cycle continues. These devices are relatively simple in their construction and also highly reliable, since they feature no moving parts. Today heat pipes are used in a variety of applications such as electronics cooling, refrigeration, air conditioning, de-icing, oil pipelines, and space radiators [1, 2]. Mueller [3] gave an overview of the history of heat pipes and their application in the nuclear industry.

One important application of heat pipes is the heat transfer in nuclear microreactors. As their name implies, microreactors are characterized by their relatively small physical size, which enables them for applications not possible with larger reactors, including remote locations and regions of temporary power needs such as those affected by natural disasters. The size of these reactors is restricted such that they can be factory-assembled and transported to site by truck, boat, plane, or train. The much smaller capital cost of these reactors provides a significant economic advantage over other next-generation nuclear reactors, which can signicantly accelerate their deployment and adoption. Heat-pipe cooled microreactors (HPMRs) utilize heat pipes to transfer heat from the reactor core to the power conversion system. A notable HPMR design under development is Westinghouse Electric Corporation's eVinci™ reactor [4].

Because of the strong physical coupling that exists between a heat pipe and the components of a heat-pipe-cooled microreactor, reliable and accurate heat pipe models are essential for HPMR modeling. Various methodologies exist for modeling heat pipe behavior in steady state and transient operation, each presenting distinct advantages and limitations depending on their level of fidelity. Lumped capacitance models and thermal network analysis use simplified heat transfer dynamics and analytic relations to predict the heat pipe performance without formal spatial discretization. Some examples are presented in [5] and [6]. These models are appropriate for design studies and potentially optimization procedures because of their quick, simple, and robust solution schemes. The effective heat conduction approach simplifies modeling by employing heat conduction equations with a very high thermal conductivity for the vapor core [7]. However, the vapor core thermal conductivity needs to be carefully adjusted to enforce the operating limits [8].

More comprehensive models simulate the fluid dynamics of the working fluid and thus have the capability to mechanistically predict the operational limits or the condenser pool effects, but these approaches demand significant computational resources due to spatial discretization in one, two, or three dimensions. Some examples include the Thermal Hydraulic Response of Heat Pipes Under Transients (THROHPUT) code [9], the Heat Pipe Transient Analysis Model (HPTAM) [10], the RELAP5 extension for heat pipes, ATHENA [11], or the two-phase flow model in Sockeye [12]. See [3] for a recent and more detailed review of the available heat pipe models.

Two-phase flow models provide the most accurate description of the physics inside of heat pipes, but they present numerous modeling challenges to achieve a robust and efficient solution for one-dimensional flow models. A common challenge in the design of two-phase models is the treatment of a vanishing phase. For example, in a heat pipe, a dry-out condition causes the liquid phase to vanish locally in the evaporator section. This example is an accident condition, so many heat pipe codes may not seek to model this event but just predict its onset instead. However, another example in a heat pipe is much more routinely occurring in a heat pipe: the formation of liquid pools, i.e., a local vanishing of the vapor phase. For horizontal heat pipes, excess working fluid tends to accumulate at the condenser end of the heat pipe, forming a "condenser pool." Heat pipes are often designed to have excess working fluid, so these pools are not uncommon. Phase disappearance can be very challenging to treat because the determination of the thermodynamic state of the vanished phase can incur significant errors due to zero or near-zero quantities (like the volume fraction of the vanished phase) involved in the calculation. Roundoff error becomes significant here, and the result is often that the computed thermodynamic state is outside of the range of validity, resulting in immediate solve failure. This depends on the implemented equation of state model(s) for the working fluid, which may or may not have sufficient artificial resilience to error in the state input. For example, simplified analytic equations of state like the ideal gas equation of state may be resilient to these errors and still provide a reasonable value for the desired property, despite erroneous input properties; however, a realistic equation of state for the liquid may not have this feature. Sockeye is provided with realistic equations of state for liquid and vapor sodium and potassium, and the phase disappearance difficulties were found in many cases for Sockeye's two-phase model described in [12]. In addition to possible robustness issues, two-phase models present a greater difficulty in model development and implementation, as well as a noticeable runtime increase, with respect to single-phase models. In addition, the phases in a heat pipe are largely segregated, making an alternative approach based on single-phase flow attractive.

This paper describes a novel method referred to as the Liquid-Conduction, Vapor-Flow (LCVF) model since the liquid phase is modeled with the heat conduction equation instead of flow equations. For the annular screened wick heat pipes that are commonly used in heat pipe microreactor applications, the liquid pressure drop is relatively simple to analyze, since the liquid phase has a very slow, laminar flow. This observation justifies the use of a simplified treatment of the liquid phase in microreactor heat pipe models.

This model was implemented in the heat pipe code Sockeye, based on MOOSE (Multiphysics Object-Oriented Simulation Environment), an open-source finite element framework that provides the foundation for numerous physics applications spanning many disciplines [13, 14]. A selection of relevant applications for multiphysics simulations in the nuclear industry include Griffin, which models radiation transport and reactor analysis [15, 16], BISON, which models thermomechanics and fuel performance [17], and DireWolf, which couples Griffin, BISON, and Sockeye for nuclear microreactor analysis [18]. Sockeye leverages the thermal hydraulics module [19] of MOOSE to assemble heat pipe models in the fashion of thermal systems codes. Since the intended application of Sockeye is for nuclear microreactors, which may feature several hundred heat pipes, high-fidelity models would be prohibitively expensive in terms of computational resources; therefore, Sockeye is designed for the "engineering scale," prioritizing computational efficiency at the expense of higher fidelity, resulting in the use of primarily one-dimensional flow models. Within the engineering scale, Sockeye features three main simulation capabilities, including a one-dimensional, two-phase model [12, 8], a two-dimensional heat conduction model [8, 20], and the LCVF model, the subject of this paper.

This paper is organized as follows: Section 2 describes the LCVF model and its sub-models, Section 3 gives some numerical demonstrations of the model, and Section 4 gives some conclusions of the work.

2. Model Description

2.1. Model Overview

In the LCVF mode, the vapor phase is modeled with a one-dimensional, compressible flow model, which is coupled to two-dimensional heat conduction for the liquid/wick and cladding regions via interfacial heat and mass transfer terms, as illustrated in Figure 1. The LCVF model also features a sub-model to predict the capillary limit, as well as capture the resulting dryout.

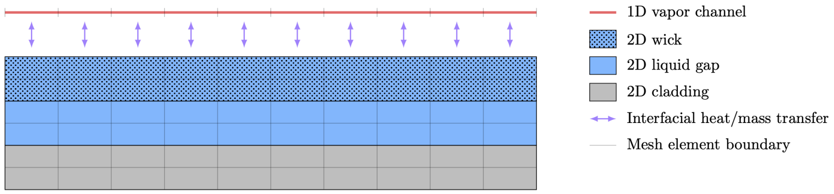

Figure 1: Illustration of the LCVF model.

2.2. Vapor Model

The vapor phase is modeled with the one-dimensional, compressible Euler equations of gas dynamics, with source terms corresponding to gravity, viscous forces, and interfacial heat and mass transfer:

$$\frac{\partial \rho_v A_v}{\partial t} + \frac{\partial \rho_v u_v A_v}{\partial x} = \Gamma_{\text{int}} A'_{\text{int}} \,, \tag{1}$$

$$\frac{\partial \rho_v u_v A_v}{\partial t} + \frac{\partial (\rho_v u_v^2 + p_v) A_v}{\partial x} = -F_v A_v + \rho_v g_x A_v \,, \tag{2}$$

$$\frac{\partial \rho_v E_v A_v}{\partial t} + \frac{\partial u_v (\rho_v E_v + p_v) A_v}{\partial x} = \rho_v u_v g_x A_v + (q_v^{\text{int}} + \Gamma_{\text{int}} E_v^{\text{int}}) A'_{\text{int}} \,, \tag{3}$$

where x is the axial heat pipe position, t is time, ρ_v is the vapor density, u_v is the vapor velocity in the x direction, p_v is the vapor pressure, E_v is the vapor specific total energy, A_v is the cross-sectional area of the vapor, Γ_{int} is the mass flux from liquid to vapor, A'_{int} is the interfacial area per unit length, g_x is the component of the acceleration due to gravity in the x direction, F_v is the vapor viscous force density, q_v^{int} is the interfacial heat flux from the interface to the vapor phase, and E_v^{int} is the vapor interfacial specific total energy. Note that the interface recession into the wick structure is neglected, and the cross-sectional area A_v is constant:

$$A_v = \frac{\pi}{4} D_{\text{wick,i}}^2 \,, \tag{4}$$

where $D_{\text{wick,i}}$ is the inner wick diameter, so the equations may be divided by this constant; however, we choose to keep the equations in this form for clarity, since some source terms are not proportional to A_v. The interfacial terms are described in Section 2.4. The viscous force density F_v is responsible for producing the correct viscous pressure drop in the vapor phase and requires definition of a friction factor f_v (here, a Darcy friction factor):

$$F_v = \frac{1}{2}\frac{f_v \rho_v u_v |u_v|}{D_{h,v}} \,, \tag{5}$$

where $D_{h,v} = D_{\text{wick,i}}$ is the vapor hydraulic diameter. Various closures may provide the definition of the friction factor. These often are functions of the axial vapor Reynolds number,

$$\text{Re}_{x,v} = \frac{\rho_v u_v D_v}{\mu_v} \,, \tag{6}$$

where μ_v is the vapor dynamic viscosity. By default, Sockeye uses the Hagen-Poiseuille equation for laminar flow ($\text{Re}_{x,v} < 2000$) and the Blasius relation for turbulent flow ($\text{Re}_{x,v} \geq 2000$) [2]:

$$f_{D,v} = \begin{cases} \frac{64}{\text{Re}_{x,v}} & \text{Re}_{x,v} < 2000 \\ \frac{0.316}{\text{Re}_{x,v}^{0.25}} & \text{Re}_{x,v} \geq 2000 \end{cases} \,, \tag{7}$$

but with a smooth transition between $\text{Re}_{x,v} = 1500$ and $\text{Re}_{x,v} = 2500$ to alleviate the discontinuity at $\text{Re}_{x,v} = 2000$.

The flow equations are discretized using a cell-centered finite volume method, using the Harten-Lax-van-Leer-Contact (HLLC) flux formulation with second-order slope reconstruction [21]. Because the working fluids inside high-temperature heat pipes are typically frozen at room temperature, vacuum or near-vacuum conditions exist inside the heat pipe until sufficient vaporization has occurred. This transient typically involves an advancing melt front, which also results in an advancing continuum vapor front, since the vapor that condenses does not make it far past the melt front. Beyond this continuum front, the vapor is largely in a rarefied gas regime, so continuum flow models are not ideal to model this region [2]. To approximate this situation, an engineering approximation is made in the above model: an interior wall boundary condition is applied to a given cell interface if either of the adjacent pressure values are below a certain threshold.

2.3. Heat Conduction Model

The wick, liquid annulus, and cladding regions are modeled with two-dimensional heat conduction with a mixture of components:

$$\sum_i \alpha_i \rho_i c_{p,i} \frac{\partial T}{\partial t} + \nabla \cdot (-k \nabla T) = q''' \,, \tag{8}$$

where i is the component index, α_i is the component volume fraction, ρ_i is the component density, $c_{p,i}$ is the component specific heat capacity, T is the mixture temperature, k is the mixture thermal conductivity, and q''' is the volumetric heat source term. The components include the working fluid liquid/solid phase, the wick material, and the cladding material. Note that below the melting temperature of the fluid, properties of the solid phase are approximated to be equal to the liquid properties evaluated at the triple point of the fluid, and also note the latent heat of fusion is neglected when crossing the melting point. Equation (8) is discretized using the continuous finite element method with first-order Lagrange elements.

Due to the high thermal conductivity of the liquid/solid phase of the working fluid and its low velocity, heat conduction is the dominant heat transfer mechanism, so the thermal resistance of the interface between the cladding and the working fluid is neglected. The exterior surface of the heat pipe cladding may be the boundary of the problem domain, in which case boundary conditions are applied, or it may be coupled to another domain, in which case some interface conditions are applied. Boundary conditions may include, for example, Dirichlet boundary conditions, adiabatic conditions, prescribed heat flux conditions, convection conditions, radiation conditions, or combination conditions. The interface conditions at the inner wick surface are described in Section 2.4.

The volumetric heat source term is zero in the cladding, but in the wick and liquid annulus regions, it is used to model advection of the liquid energy; this is described in Section 2.5.

2.4. Interfacial Coupling Model

Interfacial heat and mass transfer between the liquid and vapor phases is achieved by applying source terms to the vapor flow channel and boundary fluxes to the inner surface of the wick domain.

First we obtain several interfacial properties and quantities related to the liquid-vapor interface by solving a local Half-Riemann problem about the interface [22, 23]. However, since this model lacks details on the liquid flow field, we make some approximations. First, we assume that the interfacial pressure is equal to the vapor pressure:

$$p_{\text{int}} = p_v \,, \tag{9}$$

which is reasonable because the acoustic impedance $Z = \rho c$ of the liquid phase is much greater than that of the vapor phase: $Z_\ell \gg Z_v$. Second, we assume that the interfacial velocity is zero:

$$u_{\text{int}} = 0 \,, \tag{10}$$

which is reasonable because the liquid velocity is very small while the liquid acoustic impedance is large. With these approximations, the other relevant interfacial quantities become the following:

$$T_{\text{int}} = T_{\text{sat}}(p_{\text{int}}) \,, \tag{11}$$

$$\rho_k^{\text{int}} = \rho_k(p_{\text{int}}, T_{\text{int}}) \,, \tag{12}$$

$$v_{\ell v} = \frac{1}{\rho_v^{\text{int}}} - \frac{1}{\rho_\ell^{\text{int}}} \,, \tag{13}$$

$$h_k^{\text{int}} = h_k(p_{\text{int}}, T_{\text{int}})\,, \tag{14}$$

$$h_{\ell v} = h_v^{\text{int}} - h_\ell^{\text{int}}\,, \tag{15}$$

$$E_k^{\text{int}} = h_k^{\text{int}} - \frac{p_{\text{int}}}{\rho_k^{\text{int}}}\,, \tag{16}$$

where k is either v for the vapor phase, or ℓ for the liquid phase.

Interfacial heat transfer occurs between each phase and the liquid-vapor interface; the heat flux from the interface to the phase k is computed as

$$q_k^{\text{int}} = \mathcal{H}_k^{\text{int}}(T_{\text{int}} - T_k)\,, \tag{17}$$

where T_k is the temperature of the phase, T_{int} is the temperature of the interface, and $\mathcal{H}_k^{\text{int}}$ is the interfacial heat transfer coefficient for the phase, which is provided by a closure relation. Carey approximated the heat flux across the liquid-vapor interface using the kinetic theory of gases, assuming that the pressure and temperature differences across the phases are small [24]. By further assuming that the vapor is close to the saturation state ($T_v \approx T_{\text{int}}$), which is a reasonable assumption inside of a heat pipe [2], and also that the heat transfer coefficients for each phase are equal ($\mathcal{H}_\ell^{\text{int}} = \mathcal{H}_v^{\text{int}}$), we obtain the following closure:

$$\mathcal{H}_k^{\text{int}} = \left(\frac{2a}{2-a}\right)\left(\frac{h_{\ell v}^2}{T_v v_{\ell v}}\right)\sqrt{\frac{M_v}{2\pi R_u T_v}}\left(1 - \frac{p_v v_{\ell v}}{2 h_{\ell v}}\right)\,, \tag{18}$$

where a is the accommodation coefficient, often taken to be equal to unity, $h_{\ell v} = h_v - h_\ell$ is the latent heat of vaporization, $v_{\ell v} = v_v - v_\ell$ is the difference in specific volume, M_v is the molar mass of the working fluid, and R_u is the universal gas constant.

The interfacial area per unit length is a function of the wick geometry and the local, instantaneous fill conditions; however, we compute this quantity assuming the liquid-vapor interface resides at the wick inner surface and add up the individual pore interface areas, further assuming maximum curvature:

$$A'_{\text{int}} = \frac{2\varphi\pi D_{\text{wick,i}}}{1 + \sin\theta}\,, \tag{19}$$

where φ is the wick surface porosity, and we further assume the contact angle is at maximum curvature: $\theta = \frac{\pi}{2}$. Without this last assumption, knowledge of the liquid pressure at this point is needed to infer the curvature, which is possible with this model via the liquid pressure estimation to be described later in this section, but this is avoided for simplicity.

With these definitions made, the interfacial terms in Equations (1) and (3) are fully closed. Similar energy terms are applied to the interior surface of the heat conduction domain for the liquid phase, which effectively results in applying the following incoming heat flux on that boundary:

$$q = \frac{\left(-\Gamma_{\text{int}} E_\ell^{\text{int}} - q_\ell^{\text{int}}\right) A'_{\text{int}}}{\pi D_{\text{wick,i}}}\,. \tag{20}$$

The interfacial mass flux is computed by applying the conservation of energy to a control volume around the liquid-vapor interface and rearranging:

$$\Gamma_{\text{int}} = \frac{\mathcal{H}_\ell^{\text{int}}(T_\ell - T_{\text{int}}) + \mathcal{H}_v^{\text{int}}(T_v - T_{\text{int}})}{h_{\ell v}} \,. \tag{21}$$

2.5. Liquid Energy Advection Model

Modeling the liquid phase with heat conduction alone neglects the advection of energy, which has a much greater rate than thermal conduction; thus, we introduce a source term to approximate this effect.

When phase change occurs, mass and energy are transferred between the phases. Evaporation removes mass and energy from the liquid phase, and condensation adds mass and energy to the liquid phase. In steady conditions, the mass and energy lost in this way in the evaporator are replenished by advection of the liquid from the condenser end. Since the heat conduction equation is solved for the liquid phase, this liquid advection is not captured naturally, so this effect is approximated by adding a volumetric source term.

At the liquid-vapor interface, due to interfacial mass transfer, the rate of energy added to the liquid phase per unit axial length is $-\Gamma_{\text{int}} E_\ell^{\text{int}} A'_{\text{int}}$ (negative for evaporation and positive for condensation). Due to the circulation of the working fluid, this source should be offset by an equal and opposite source. However, since advection occurs throughout the wick/annulus volume, rather than on the surface like phase change, the source is distributed uniformly in the wick and annulus at a given axial position:

$$q''' = \frac{\Gamma_{\text{int}} E_\ell^{\text{int}} A'_{\text{int}}}{A_{\text{wick}} + A_{\text{ann}}} f \,, \tag{22}$$

where f is a normalization factor. To conserve energy, the volume integral of this term must be zero. To accomplish this, we first define the positive and negative integrals of $-\Gamma_{\text{int}} E_\ell^{\text{int}} A'_{\text{int}}$:

$$\dot{E}^+ = \int_0^{L_{\text{hp}}} \max\left(-\Gamma_{\text{int}} E_\ell^{\text{int}} A'_{\text{int}}, 0\right) \, dx \,, \tag{23}$$

$$\dot{E}^- = \int_0^{L_{\text{hp}}} \min\left(-\Gamma_{\text{int}} E_\ell^{\text{int}} A'_{\text{int}}, 0\right) \, dx \,, \tag{24}$$

Then we compute a normalization factor f^+ as

$$f^+ = \frac{-\dot{E}^-}{\dot{E}^+} \,, \tag{25}$$

which when applied to the positive integral, gives the desired result for energy conservation: $\dot{E}^+ f^+ + \dot{E}^- = 0$. Thus f in Equation (22) is the following:

$$f = \begin{cases} f^+ & -\Gamma_{\text{int}} E_\ell^{\text{int}} A'_{\text{int}} > 0 \\ 1 & -\Gamma_{\text{int}} E_\ell^{\text{int}} A'_{\text{int}} \leq 0 \end{cases} \,. \tag{26}$$

Note that to achieve better nonlinear convergence, this term is evaluated at the old time step solution. The normalization factor requires an integral over the axial length. Thus computing this normalization factor with the current solution would introduce Jacobian contributions from degrees of freedom on the vapor and liquid side, along the entire length, which is undesirable because it increases the coupling stencil of the Jacobian matrix. Neglecting the contributions from this normalization factor was found to increase the number of nonlinear iterations required. Therefore, this was avoided by evaluating the source term at the old solution.

2.6. Evaporator Mass Model

During normal, steady operation of a heat pipe, the working fluid mass distribution is expected to be relatively stable, with the liquid phase approximately filling the wick and any excess tending to form a pool at the condenser end. In the evaporator, the liquid evaporates at some rate and is replenished at the same rate by advection from the condenser end. However, if the rates are imbalanced, such as when the power is above the capillary limit, the working fluid inventory in the evaporator section depletes, possibly completely if no intervention is taken, such as reducing the applied power. To mechanistically capture this type of event, a two-phase flow model is recommended; however, in the context of the LCVF model, we employ a semi-mechanistic approach, which is described in this section.

For a given time step, we first make a semi-analytic determination of whether the capillary limit is exceeded. This limit is derived theoretically by comparing the sum of the various pressure drops Δp_j around the circuit, such as the vapor pressure drops, liquid pressure drops, and the evaporation/condensation pressure drops, to the maximum capillary pressure, $\Delta p_{\text{cap,max}}$ [2, 1]. For a given operating temperature T, the capillary limit power is the maximum power $\dot{Q}$ such that the following is true:

$$\sum_j \Delta p_j(\dot{Q}, T) \leq \Delta p_{\text{cap,max}} \,. \tag{27}$$

However, there is some dependency between the liquid and vapor pressures, so the individual pressure drops may not be able to be computed independently in this manner; therefore we use a generalized version of the capillary limit condition:

$$\max_x (p_v(x) - p_\ell(x)) \leq \Delta p_{\text{cap,max}} \,. \tag{28}$$

The maximum capillary pressure for a heat pipe requires geometric and material information about the wick structure; typically this information is summarized by an experimentally-determined value called the effective pore radius R_{pore}, such that for a temperature T, the maximum capillary pressure is computed as

$$\Delta p_{\text{cap,max}} = \frac{2\sigma(T)}{R_{\text{pore}}} \,, \tag{29}$$

where σ is the surface tension of the fluid. This maximum capillary pressure expression ($2\sigma/R$) corresponds to the capillary pressure across a hemispherical (maximum curvature) interface of radius R. Real wicks have a distribution of pore sites of varying pore geometries, so the effective pore radius is representative of the actual distribution, not necessarily the actual pore sizes.

The vapor flow equations yield the vapor pressure distribution, but since the liquid flow equations are not solved, we lack the liquid pressure distribution, so we must estimate it. To do this, we make steady assumptions so that we can use analytic solutions, which assume a uniform power distribution in the evaporator and condenser, and a uniform liquid temperature. For a homogeneous wick, i.e., no gap between the wick and the wall, Darcy's law is appropriate:

$$\frac{dp_\ell}{dx} = -\frac{\mu_\ell u_\ell(x)}{K} = -\frac{\mu_\ell \dot{m}_\ell(x)}{\rho_\ell A_\ell K} = \frac{\mu_\ell \dot{Q}(x)}{\rho_\ell h_{\ell v} A_\ell K}\,, \tag{30}$$

where μ_ℓ is the liquid dynamic viscosity, u_ℓ is the liquid velocity, K is the wick permeability, $\dot{m}_\ell$ is the liquid mass flow rate, A_ℓ is the liquid cross-sectional area, and $\dot{Q}(x)$ is the integral of the linear heat rate. Note that we use the notation $\dot{Q}$ without the x argument to denote the maximum value, attained at the evaporator exit. For a wick with a gap, the vast majority of the flow goes through the gap rather than the wick, so an annular flow approximation is appropriate to estimate the pressure drop:

$$\frac{dp_\ell}{dx} = f_\ell \frac{\rho_\ell u_\ell(x)^2}{2D_{h,\ell}}\,, \tag{31}$$

where $D_{h,\ell} = 2t_{\text{ann}}$ is the hydraulic diameter of the liquid flow through the annular gap of thickness t_{ann} and f_ℓ is the friction factor according to Hagen-Poiseuille's theory for fully developed flows in concentric annuli [25]:

$$f_\ell = \frac{64}{\text{Re}}\zeta\,, \tag{32}$$

where ζ is a factor depending on the inner and outer radii of the annulus but quickly approaches the value 2/3 in the thin-annulus limit. Integrating one of these liquid pressure gradients gives the liquid pressure drop distribution, and then the absolute liquid pressure distribution is determined by translating the liquid pressure drop distribution such that the liquid and vapor pressures are equal at the expected wet point. For horizontal heat pipes, the wet point is located at the condenser end. Lastly, we perform a sweep from the wet point to correct the condition $p_\ell > p_v$. This is possible because the vapor phase can actually have a net negative pressure drop due to inertial pressure recovery, but it is an unstable condition, since the convex interface tends to be sheared by the vapor flow. To correct this condition, the liquid pressure is set equal to the vapor pressure at that point, and subsequent liquid pressure drops in the sweep are applied from that point. With both phasic pressure distributions calculated, the capillary limit condition expressed in Equation (28) can be checked.

To attempt to capture the capillary limit effect, we add an ordinary differential equation to the system, corresponding to the conservation of mass in a control volume containing the evaporator section of the wick and liquid gap. When the capillary limit condition *is not* violated, we assume that any working fluid that is lost to evaporation is exactly compensated, so a steady value for $M_{\ell,\mathrm{e}}$, the liquid mass in the evaporator section, is held:

$$M_{\ell,\mathrm{e}} = M_{\ell,\mathrm{e,max}} \,, \tag{33}$$

where $M_{\ell,\mathrm{e,max}}$ corresponds to the mass that exactly fills the wick in the evaporator section at the given temperature. When the capillary limit condition *is* violated, we let the mass deplete by the evaporation rate, and conservatively assume that no mass is gained by advection into the evaporator section:

$$\frac{dM_{\ell s,\mathrm{e}}}{dt} = \int\limits_{0}^{L_{\mathrm{evap}}} -\Gamma_{\mathrm{int}} A'_{\mathrm{int}} \, dx \,. \tag{34}$$

The variable $M_{\ell,\mathrm{e}}$ is used in the computation of the volume fractions in Equation (8), and also whenever $M_{\ell s,\mathrm{e}}$ is zero, interfacial heat and mass transfer is disabled, which leads to a heatup of the wick and cladding regions.

2.7. Inactive Length Model

Working fluid in excess of that which fills the wick completely is often included by design, to ensure a proper wet point for capillary pressure. However, this excess working fluid alters the temperature distribution in the heat pipe because this excess tends to form a pool at the condenser end of the heat pipe (at least in the horizontal orientation), which reduces the length over which the vapor can condense and thus decreases the rate at which heat can be removed in the condenser for a given operating temperature. Additionally, sometimes non-condensable gases (NCGs) are introduced into the heat pipe, either intentionally or unintentionally, which have a similar effect since these also tend to accumulate in a pool at the condenser end. To capture the resulting effect on heat transfer mechanistically requires a two-phase model, so an approximation must be made for the LCVF model.

Using the equations of state of the working fluid and the NCG(s) and the known masses of each, the lengths of these pools (L_{pool} and L_{ncg}, respectively) can be computed and summed to give the total inactive length in the condenser:

$$L_{\mathrm{cond,inactive}} = L_{\mathrm{pool}} + L_{\mathrm{ncg}} \,. \tag{35}$$

To approximate the effect of an inactive length in the vapor channel, we dynamically implement an interior wall boundary condition at the cell boundary at or immediately upstream of the position $x = L_{\mathrm{hp}} - L_{\mathrm{cond,inactive}}$, where x is the distance from the evaporator end, and L_{hp} is the total heat pipe length. To create smooth transitions between cell boundaries with a moving pool front location, the open flow area of the upstream cell interface of the cell containing the pool front is linearly interpolated.

3. Numerical Demonstrations

In this section, numerical demonstrations of the LCVF model are given with several verification and validation test problems.

In all cases, Newton's method is used to solve the nonlinear systems of equations resulting from spatial and temporal integration of the governing equations. These problems are temporally discretized with the second-order Backward Difference Formula (BDF-2) method, which is implicit and A-stable [26]. Unless otherwise stated, time step sizes are chosen adaptively by seeking a target number of nonlinear iterations (usually 5) for each time step.

3.1. Capillary Limit Study

One of the primary goals of a heat pipe analysis tool is to accurately predict the capillary limit of heat pipe operation. This limit characterizes the capillary pumping power of the heat pipe, measuring its ability to continue operation under certain heat input and temperature conditions. When this limit is exceeded, the evaporator section can dry out until some intervention takes place.

In this section we test whether Sockeye's LCVF model is able to reproduce a capillary limit curve. Since experimental data on the capillary limit of high-temperature heat pipes is relatively scarce, we compare it to an analytic capillary limit curve. This curve can be derived with Equation (28) with steady-state pressure distributions. The liquid pressure distribution can be derived by integrating Equation (30) or (31), and the vapor pressure distribution can be derived using theories such as that of Cotter [27] or Busse [28]. In this study, we use the Cotter analytic solution, since the Busse solution is limited to relatively small radial Reynolds numbers.

Since the dominant pressure drop (liquid vs. vapor) depends on the type of wick considered, we study two representative heat pipes. The annular-wick heat pipe is summarized in Table 1, and the homogeneous-wick heat pipe is the same except that its outer wick diameter is set to the inner cladding diameter: $D_{\text{wick,o}} = D_{\text{clad,i}}$. The working fluid fill ratio is defined as the ratio of the working fluid volume V_{fluid} to the maximum fluid volume for the wick and annulus regions, $V_{\text{wick,ann}}$. Since liquid density (and thus V_{fluid}) varies with temperature, the fill ratio is listed with the used reference temperature. In this study we use the operating temperature used in each run, T_{op}. Note that the cladding was not included since we are not concerned with any transient accuracy for this study. The numbers of axial elements used in the evaporator, adiabatics, and condenser sections were 30, 20, and 30, respectively, and 4 radial elements were used in the wick.

Sockeye runs were performed at 5 different operating temperatures (1000 K, 1100 K, 1200 K, 1300 K, and 1400 K). These temperatures are chosen to be large enough that the sonic limit does not interfere with the study. In each run, the initial temperature was set to the operating temperature value, and then uniform heat fluxes were applied to the evaporator and condenser sections, with the net heat rate into the system being zero at all times, so that the initial energy of the system is preserved, only allowing for some small temperature

Table 1: Annular-wick heat pipe specifications for the capillary limit study.

Parameter	**Value**
Orientation	Horizontal
Working fluid	Sodium
Working fluid fill ratio, $V_{\text{fluid}}/V_{\text{wick,ann}}$	1 at T_{op}
Wick inner diameter, $D_{\text{wick,i}}$	0.01231 m
Wick outer diameter, $D_{\text{wick,o}}$	0.01300 m
Cladding inner diameter, $D_{\text{clad,i}}$	0.01410 m
Evaporator length, L_{evap}	0.3 m
Adiabatic length, L_{adia}	0.2 m
Condenser length, L_{cond}	0.3 m
Wick porosity, φ	0.7
Effective pore radius, R_{pore}	20×10^{-6} m
Wick permeability, K	10^{-10} m^2

redistribution about the nominal operating temperature value. The power was slowly ramped up from zero, and at the end of each time step, the capillary limit condition given by Equation (28) was checked, and when it is reached, the simulation is terminated, and the current temperature and power are plotted.

Figure 2 shows the capillary limit results for the homogeneous-wick heat pipe. The Sockeye results match the curve very well, which is expected because for this wick type, the liquid pressure drop dominates, and the liquid pressure drop for the LCVF model uses the same analytic formulation that the analytic capillary limit uses. Figure 3 compares the computed pressure distributions against the analytic pressure distributions for this heat pipe for a power of 1 kW at an operating temperature of 1200 K, which shows that the distributions are visually indistinguishable.

Figure 4 shows the capillary limit results for the annular-wick heat pipe case. The Sockeye results still match fairly well, but in this case there is a noticeable discrepancy. Note how much greater the capillary limit is for this heat pipe compared to the homogeneous-wick heat pipe: this illustrates the significant design advantage of incorporating a gap between the wick and the wall, as it allows the liquid to take a path of much smaller pressure drop. In this case, the vapor pressure drop is the dominant component of the capillary limit, so the ability to match the analytic solutions is largely determined by which of the models is chosen by the vapor flow model and if they match the analytic solution's models.

To examine the vapor pressure drop component in greater detail, we consider a single case, with a power of 20 kW and an operating temperature of 1200 K. The pressure distributions computed by Sockeye is compared to the analytic pressure drop distributions, where the vapor distribution is computed using Cotter's theory [27].

In addition, Nek5000, an open-source spectral-element code [29], was used to

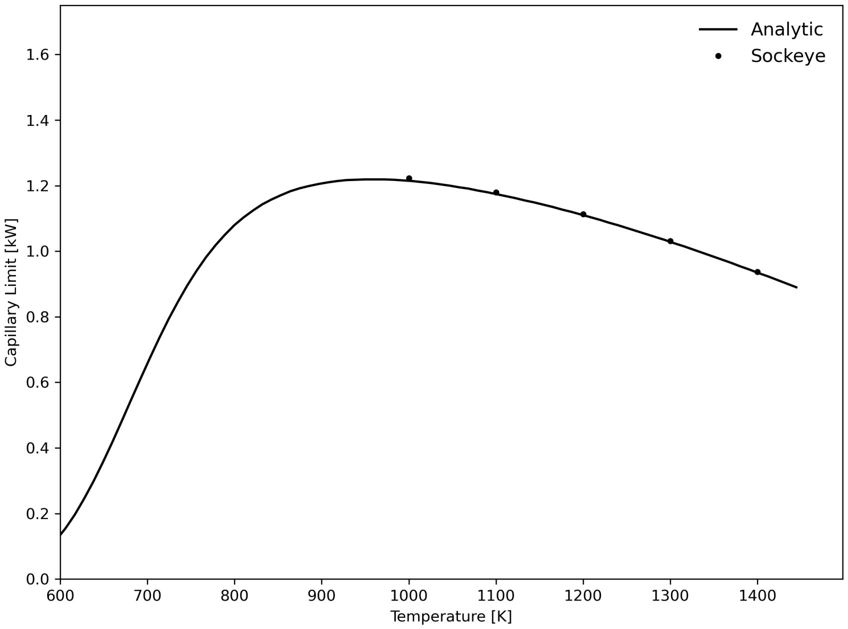

Figure 2: Comparison of computed capillary limit against analytic limit for the homogeneous-wick heat pipe.

simulate the heat pipe's vapor core with a 2D axisymmetric model. The mesh was comprised of 6,400 elements, with a refinement near the wall to account for boundary layer effects. The solution was approximated by the tensor-product of Nth-order Lagrange polynomials P_N, resulting in $(N+1)^2$ Gauss-Lobatto-Legendre (GLL) grid points within each element. An optimum polynomial order of $P_N = 5$ was chosen to conduct the simulations. The model incorporated the following boundary conditions:

1. Uniform inlet boundary conditions for mass injection and extraction at the radial boundary of the evaporator and condenser sections.
2. No-slip boundary conditions at the radial boundary of the adiabatic section, as well as the two axial boundaries.

The unsteady simulations were conducted using the RANS $k-\tau$ turbulence model [30]. The simulations were run for one flow-through, and the results were time-averaged and then spatially averaged in the radial direction to compare with the Sockeye results.

Figure 5 compares Sockeye's computed pressure distributions against the analytic pressure distributions and Nek5000. Cotter's solution for the vapor pressure drop effectively uses the Hagen-Poiseuille equation for the viscous pressure gradient,

$$f_{D,v} = \frac{64}{\mathrm{Re}_{x,v}} \,, \tag{36}$$

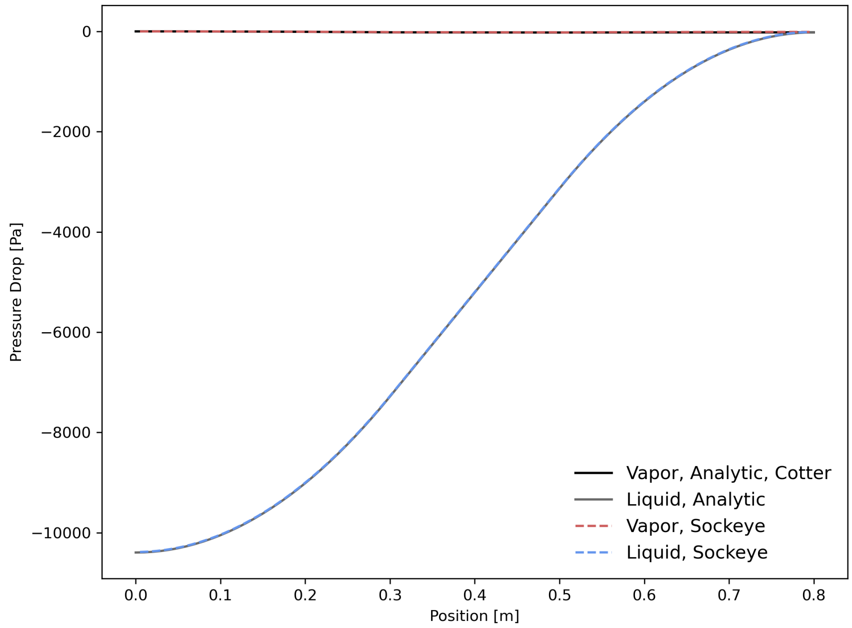

Figure 3: Comparison of computed pressure distributions against analytic pressure distributions for the homogeneous-wick heat pipe for a power of 1 kW and temperature of 1200 K.

whereas the closure used in Sockeye, given by Equation (7), switches to the Blasius relation for the higher Reynolds number in this problem. For the inertial pressure drop, Cotter used a pressure gradient obtained by Knight and McInteer for flow between porous walls with suction or injection, and in the condenser section, used a different velocity profile, which leads to a pressure recovery fraction of $\frac{4}{\pi^2}$, whereas other theories predict a full inertial pressure recovery [1]. The Nek5000 solution matches the analytic evaporator pressure drop and gives a total pressure recovery that lies between Cotter's prediction and Sockeye's prediction. Based on these results, Sockeye over-predicts the total pressure recovery. The condenser pressure drop is the main source of discrepancy between various models, but it is important to observe from an example like Figure 4 that under the assumptions of the $p_\ell > p_v$ correction mentioned in Section 2.6, the condenser pressure drop is not relevant for the prediction of the capillary limit of horizontal heat pipes with the condenser pressure recovery exceeding the liquid pressure drop, since the wet point moves to the condenser entrance.

Lastly, as some verification, in Figure 6 we compare the computed mass flow rate distribution with the analytic and Nek5000 mass flow rate distributions for the same case (20 kW, 1200 K), where the results are visually indistinguishable.

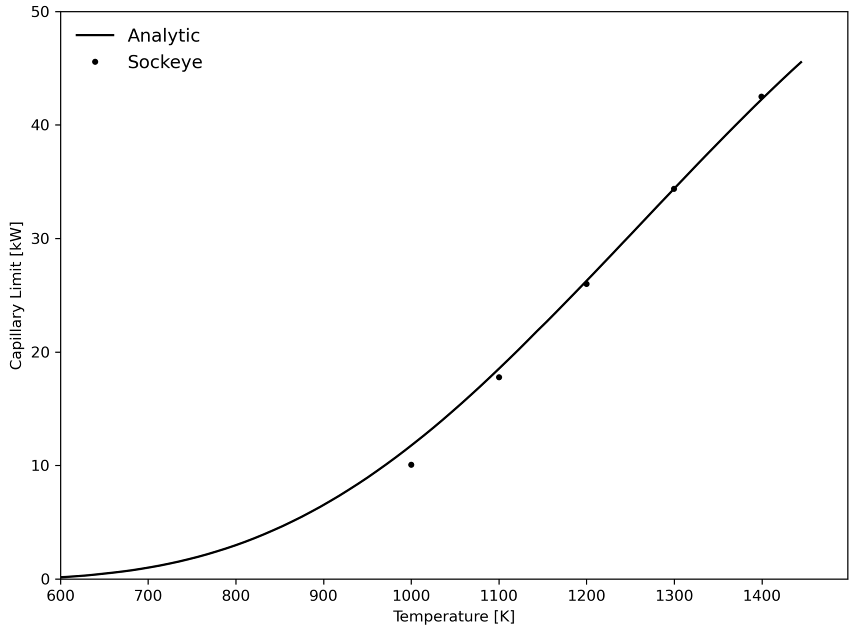

Figure 4: Comparison of computed capillary limit against analytic capillary limit for the annular-wick heat pipe.

3.2. Sonic Limit Study

The sonic limit is regularly encountered in the startup of high-temperature heat pipes since it is very small at low temperatures. The limit does not represent a serious failure of the system; rather, it represents a temporary condition that resolves itself naturally, since the result of exceeding a limit is an increase of temperature, and the sonic limit rises sharply with increasing temperature.

In this section we demonstrate that Sockeye's LCVF model is able to reproduce a sonic limit curve. An analytic curve can be derived by considering the steady, one-dimensional vapor flow equations without friction terms, using the perfect gas assumption, assuming uniform heating conditions in the evaporator, and finding the power at which the Mach number Ma is unity [2]:

$$\dot{Q}_{\text{sonic}}(T) = \frac{\rho_v(T) c_v(T) h_{\ell v}(T) A_v}{\sqrt{2(\gamma_v + 1)}} \,, \tag{37}$$

where c_v is the sound speed and γ_v is the ratio of specific heat capacities, $c_{p,v}/c_{v,v}$.

The heat pipe considered in this study is described in Table 2. The effective pore radius and wick permeability were chosen as such to avoid any interference by the capillary limit. As with the capillary limit study, the cladding was also omitted. The numbers of axial elements used in the evaporator, adiabatics, and

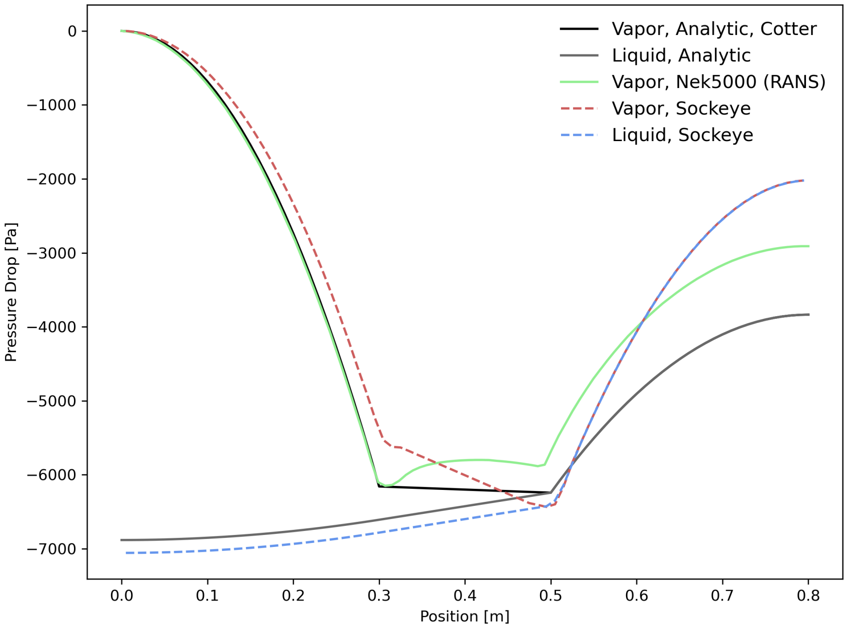

Figure 5: Comparison of computed pressure distributions against analytic pressure distributions for the annular-wick heat pipe.

condenser sections were 30, 20, and 30, respectively, and 3 radial elements were used in the wick.

Table 2: Heat pipe specifications for the sonic limit study.

Parameter	**Value**
Orientation	Horizontal
Working fluid	Sodium
Working fluid fill ratio, $V_{\text{fluid}}/V_{\text{wick,ann}}$	1 at T_{op}
Wick inner diameter, $D_{\text{wick,i}}$	0.01231 m
Wick outer diameter, $D_{\text{wick,o}}$	0.01410 m
Cladding inner diameter, $D_{\text{clad,i}}$	0.01410 m
Evaporator length, L_{evap}	0.3 m
Adiabatic length, L_{adia}	0.2 m
Condenser length, L_{cond}	0.3 m
Wick porosity, φ	0.7
Effective Pore radius, R_{pore}	10×10^{-6} m
Wick permeability, K	1 m^2

Sockeye runs were performed in the same manner as in the capillary limit

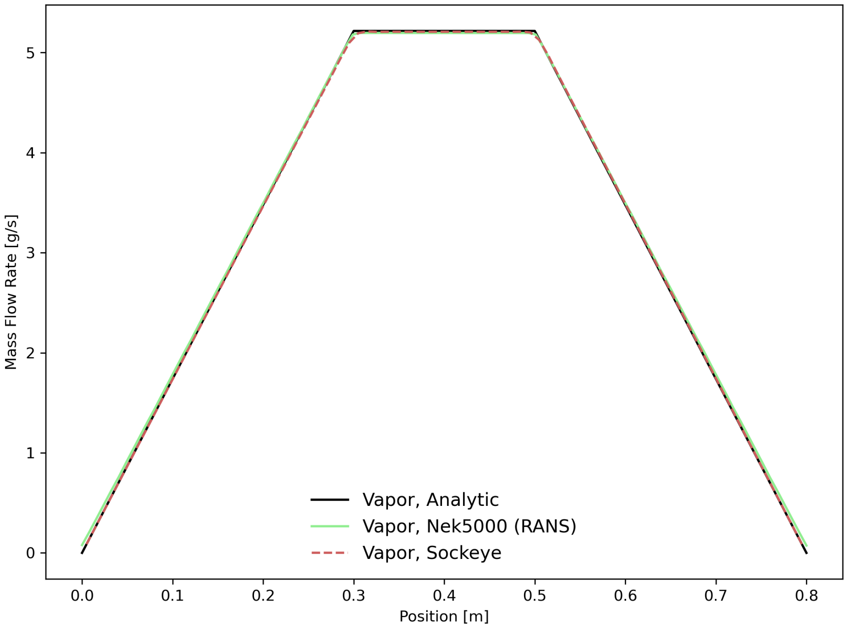

Figure 6: Comparison of computed mass flow rate distributions against analytic mass flow rate distributions for the annular-wick heat pipe.

study, at the temperatures 800 K, 850 K, 900 K, and 950 K. The only difference in procedure was that the termination condition became the presence of any sonic or supersonic flow:

$$\max_{x} \mathrm{Ma}(x) \geq 1\,. \tag{38}$$

Figure 7 shows the comparison between the computed sonic limit and the analytic sonic limit, which shows excellent agreement and serves as a verification of the compressible flow model.

3.3. Steady-state validation against Ivanovskii's heat pipe experiments

Ivanovskii et al. [31] performed many experiments at a variety of powers and cooling conditions, with a sodium heat pipe using a mesh screen wick with an annular gap. For each case, the steady vapor temperature distribution was measured using a movable micro-thermocouple. Here we consider one of these cases, where the power applied to the heat pipe was 615 W, and the operating temperature was roughly 823 K.

Table 3 gives the heat pipe specifications for this case. There were several quantities which were not provided in [31]; these are estimated and listed as "Unknown" in the table. Additionally, the presence of non-condensable gases in the heat pipe is unknown. The cladding composition and thickness are also unknown, but the cladding layer can be neglected without much error for a

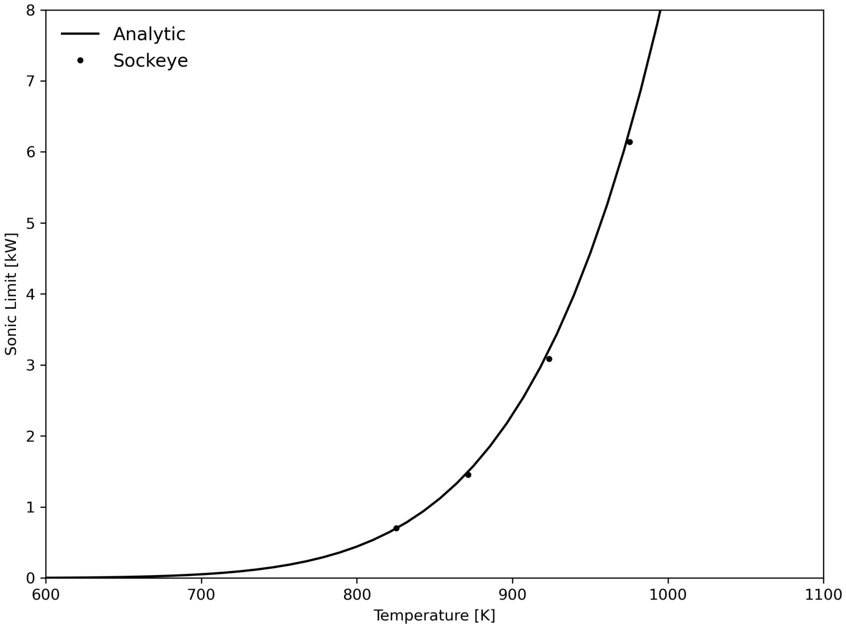

Figure 7: Comparison of computed sonic limit against analytic sonic limit.

steady study. Also note that the experimental data is indicative of effects that shorten the active condenser length of the heat pipe, such as the presence of non-condensable gases or a pool of excess working fluid. Since the origin is unknown, we take the approach taken in [32] and directly shorten the condenser length to be 25 cm.

Without specific knowledge of the heating and cooling mechanisms, the power is applied uniformly along the outer surface of the liquid layer in the evaporator length, and a convection heat flux q is applied to the condenser length:

$$q = h(T_\infty - T)\,, \tag{39}$$

where T is the heat pipe surface temperature, T_∞ is the external temperature, set to be 300 K, and h is the heat transfer coefficient, determined to be 95.4 W/(m^2-K) by trial and error to match the operating temperature.

The case was simulated with a uniform axial element length of 0.5 cm, giving 20, 10, and 50 elements for the evaporator, adiabatic, and condenser sections, respectively. The wick and annular gap regions were each discretized with two radial elements. The simulation was run using an adaptive time-stepping scheme until steady conditions were reached. Figure 8 shows the steady vapor temperature results compared against the experimental data, which shows excellent agreement. The pressure drops in each region match well, suggesting that both the viscous and inertial pressure drop terms are accurate for this particular

Table 3: Ivanovskii test case heat pipe specifications.

Parameter	**Value**	**Notes**
Orientation	Horizontal	
Working fluid	Sodium	
Working fluid fill ratio, $V_{\text{fluid}}/V_{\text{wick,ann}}$	1.01 at 500 K	Unknown
Wick inner diameter, $D_{\text{wick,i}}$	1.4 cm	
Wick thickness, t_{wick}	0.4 mm	Unknown
Liquid annular gap thickness, t_{ann}	0.5 mm	
Evaporator length, L_{evap}	10 cm	
Adiabatic length, L_{adia}	5 cm	
Condenser length, L_{cond}	55 cm	Active length $\approx$ 25 cm
Wick surface porosity, φ	0.33	
Effective pore radius, R_{pore}	0.45 mm	
Wick permeability, K	10^{-9} m^2	Unknown

regime and heat pipe. This particular case shows a high pressure recovery, which indicates that the inertial effects are dominant.

3.4. Transient validation against SAFE-30 experiments

The Safe, Affordable 30-kW Fission Engine (SAFE-30) was a space fission system that utilized heat pipes [33]. A heat pipe module was constructed for testing this reactor prototype, which consisted of a single sodium heat pipe coupled to four cylindrical tubes in which cartridge heaters were inserted [34]. The heat pipe specifications are given in Table 4. Note that the permeability was not known, so a representative value was chosen [2]. The test module was enclosed in a vacuum chamber so that only radiation boundary conditions exist at the surface, and the room enclosing the chamber was at room temperature.

The experiment ran for 7 hours, consisting of a frozen startup from room temperature, ramping up the power to a steady value, holding this value, and then ramping the power back down to zero. For simplicity, the system was approximated as a two-dimensional system, despite its azimuthal asymmetry, due to having four discrete heaters coupled to the heat pipe. This approximation was accomplished by homogenizing the heaters into a cylindrical region surrounding the heat pipe, preserving the total heat capacity. Due to the vacuum conditions, the heat transfer out of the system was due to radiation alone; the heat flux from the system boundary is the following:

$$q = \epsilon\sigma(T^4 - T_\infty^4)\,, \tag{40}$$

where T is the boundary temperature, T_∞ is the environment temperature (room temperature), σ is the Stefan-Boltzmann constant, and ϵ is the emissivity of the surface, which was taken to be equal to 0.4 for both the heat pipe

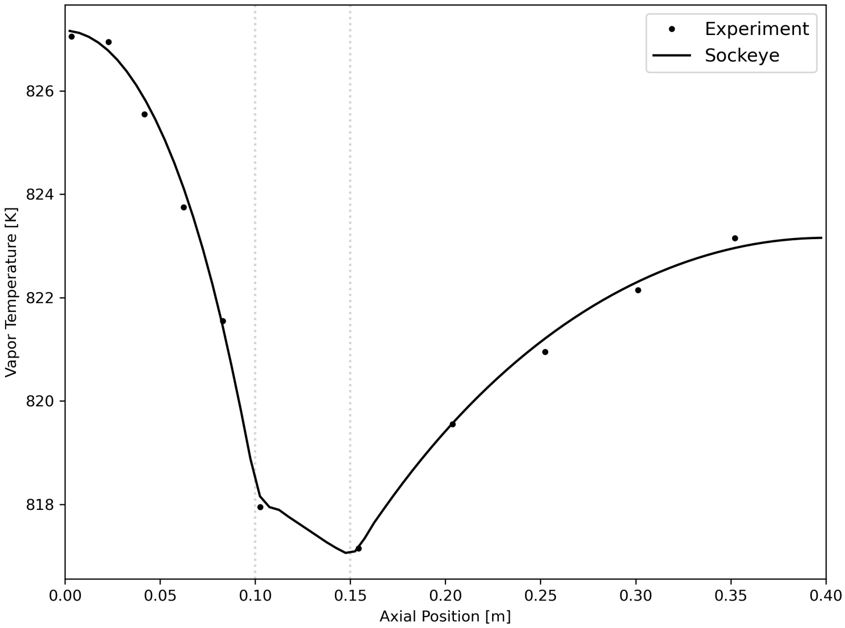

Figure 8: Comparison of computed steady vapor temperature solution against experimental data for the 615 W case by Ivanovskii. Experimental data was extracted digitally from [31].

Table 4: SAFE-30 heat pipe description.

Parameter	**Value**
Orientation	Horizontal
Working fluid	Sodium
Working fluid mass, m	0.1453 kg
Wick inner diameter, $D_{\text{wick,i}}$	0.0174 m
Wick outer diameter, $D_{\text{wick,o}}$	0.0207 m
Cladding inner diameter, $D_{\text{clad,i}}$	0.0221 m
Cladding outer diameter, $D_{\text{clad,o}}$	0.0254 m
Evaporator length, L_{evap}	0.43 m
Condenser length, L_{cond}	0.77 m
Wick porosity, φ	0.807308741
Effective pore radius, R_{pore}	47×10^{-6} m
Wick permeability, K	10^{-10} m^2

and the heaters. The coupling between the heat pipe and heaters was modeled without any resistance through the gap; a convection condition with an arbitrarily high heat transfer coefficient was used to couple these two cylindrical regions.

This experiment was previously modeled with Sockeye's other two heat pipe models, which include a two-phase flow model and a conduction model [12, 8]. The two-phase model could only simulate a fraction of the transient for a variety of factors, including the lack of sufficient state space for the equation of state in the (frozen) low-temperature, low-pressure regime, and also phase disappearance difficulties associated with the formation of a pool at the condenser end of the heat pipe. For example, starting the model at time $t = 7,500$ s, in this work, the simulation only proceeds until $t = 7,715$ s, when a condenser pool forms, so the results are not shown here. However, note that previous efforts with the two-phase model and various input combinations have been able to simulate up to $t = 18,000$ s [8]. This discrepancy illustrates the lack of reliability of the two-phase model in overcoming phase disappearance difficulties. The conduction model modeled the full transient robustly, but its accuracy during sonic-limited operation was lacking. These results are shown in Figure 9, where TC1 through TC5 correspond to thermocouples at the outer surface of the heat pipe cladding, at distances from the evaporator end of 0.216 m, 0.508 m, 0.711 m, 0.914 m, and 1.090 m, respectively. Modeling this experiment with the LCVF model avoided the phase disappearance issues of the two-phase model and improved the accuracy during startup with respect to the conduction model, while still providing a robust solution. The LCVF results are shown in Figure 10, which include results with and without the treatment of the condenser pool described in Section 2.7.

Sockeye's LCVF model captures the startup relatively well for the evaporator side of the heat pipe, but for the condenser side, the Sockeye temperatures are delayed in their rise. After the frozen startup phase, the near-isothermal condition is achieved at approximately the same time, although we note that thermocouple TC5 was just at the beginning of the condenser pool, so its temperature was a bit colder than the others in the experiment. The steady, full-power portion of the transient indicated good agreement between Sockeye results and the data, but during the ramp down, the Sockeye temperatures spread a bit more than in the experiment for both the conduction and LCVF models. This is likely a consequence of the two-dimensional approximation of the problem, since the radiative heat losses depend strongly on the azimuthal position around the heat pipe. Comparing the solutions with and without the pool treatment, we see little or no difference in the solution during startup and shutdown, but at the higher operating temperatures, we see notable differences. Figure 11 shows a zoom of Figure 10 between 8,000 s and 14,000 s. Note that for the "No pool" case, TC2 through TC5 overlap, and for the case with the pool, TC2 through TC4 overlap. While the average temperature across the heat pipe appears roughly the same with and without the pool treatment, there is a larger temperature drop across the heat pipe when the pool is modeled, leading to an evaporator temperature that is roughly 8 K higher. This larger temperature gradient is also reflected in the experimental data around 12,000 s.

The various discrepancies are attributed to several factors. First, the frozen startup modeling is very approximate, since the LCVF model is not explicitly

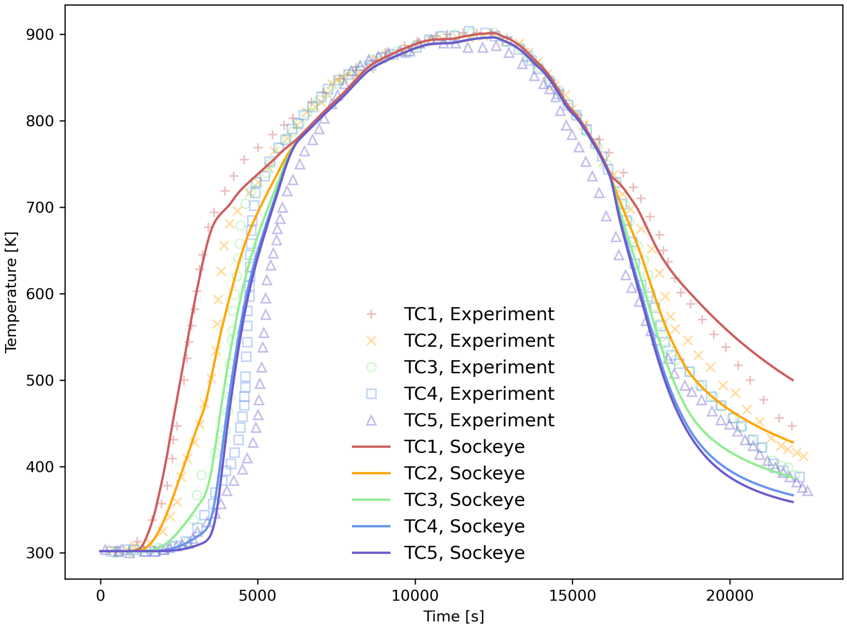

Figure 9: Comparison of computed transient temperature solution using Sockeye's conduction model against experimental data for SAFE-30.

modeling the melt front. Additionally, the vapor flow model itself is not appropriate during frozen startup since the near-vacuum conditions imply that the vapor is in a rarefied gas regime rather than a continuum regime. Second, the system was approximated as two-dimensional despite being very three-dimensional in nature. A three-dimensional model that explicitly models each cartridge heater in its actual position and performs radiative heat transfer between all of the bodies would greatly improve the model of this experiment.

Lastly, for the three Sockeye models, we compare the performance in Table 5. For the LCVF model, results are shown with and without the condenser pool modeled. First to compare robustness for this test, we compare the number of time step size reductions for each case. With the pool treatment, the LCVF model was not perfect in this metric, featuring 24 reductions. These started around $t = 5,680$ s, corresponding to a point near the end of the startup phase where heat-up of the heat pipe has caused thermal expansion of the condenser pool, causing movement of the internal wall boundary discussed in Section 2.7. The conduction model did not feature any time step size reductions, whereas the two-phase model featured 520 time steps, despite being in a much smaller simulated time range. The LCVF model was able to run with large time steps for the vast majority of the transient (the entirety of the transient if not modeling the pool), whereas the two-phase model had an average time step size of 0.21 s, due to various convergence difficulties. Overall, the LCVF had a very inter-

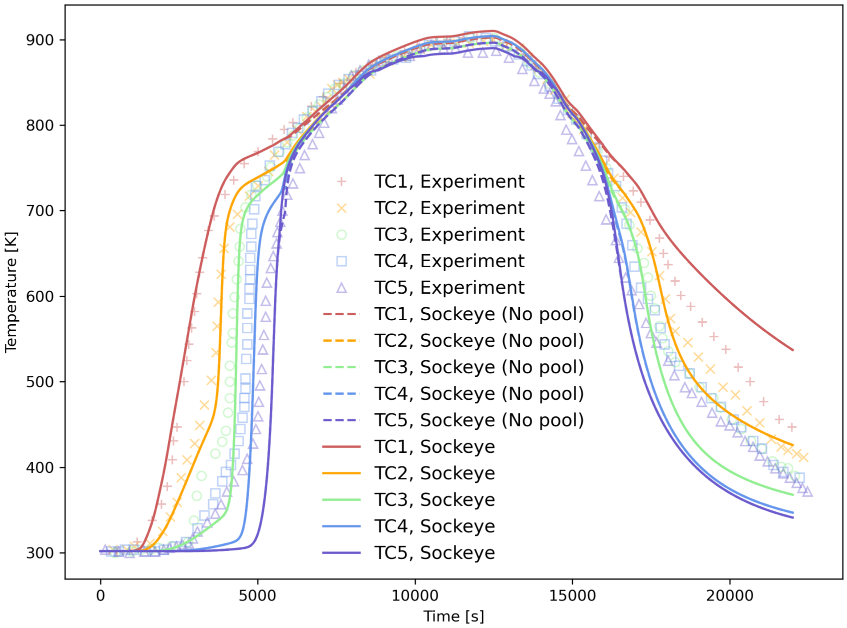

Figure 10: Comparison of computed transient temperature solution using Sockeye's LCVF model against experimental data for SAFE-30.

mediate simulation speed between the conduction model and two-phase model, as shown in the "Simulation time/wall time" metric. Unsurprisingly, the conduction model is the clear winner in terms of robustness and performance, since it is only solving the heat conduction equation, but the LCVF demonstrates comparable performance, while providing a much more accurate solution.

4. Conclusions

A heat pipe model utilizing a one-dimensional, single-phase, compressible flow model for the vapor phase, coupled to a two-dimensional heat conduction model for the liquid phase, was developed and implemented in the code Sockeye. Despite using a heat conduction model in the wick, the model is able to capture the energy transfer due to advection using a volumetric source term. The sonic limit is captured mechanistically due to the compressible flow model, and the capillary limit is captured semi-mechanistically by pairing the vapor pressure distribution with an analytically-computed liquid pressure drop distribution. This heat pipe model was verified to match analytic capillary and sonic limit curves very well, as well as analytic, steady velocity and pressure distributions. Comparisons were also made to experimental data, which showed fair agreement. Numerical experiments so far have proven the heat pipe model to be very robust,

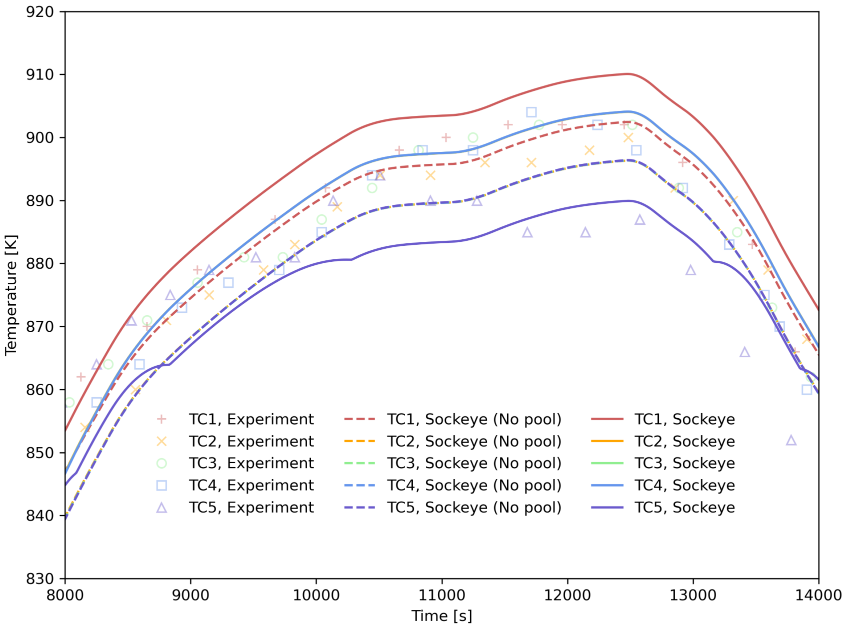

Figure 11: Comparison of computed transient temperature solution using Sockeye's LCVF model against experimental data for SAFE-30, from 8,000 s to 14,000 s.

allowing for transients that involve frozen startup, sonic-limited (supersonic) flow, and heat pipe shutdown.

Future work for this model will include extensive validation. A wealth of high-resolution heat pipe data has been produced recently, and there still exists a large amount of older heat pipe data that may prove useful. Previously-run validation cases such as SAFE-30 can benefit from more work, such as using three-dimensional heat transfer models where the system lacks azimuthal symmetry. Validation efforts will reveal the shortcomings of this model and inform the priorities for model improvement. The main area already known to need improvement is the accuracy of frozen startup, since many questionable model approximations have been made. Lastly, multiphysics coupling efforts are already underway, and a paper on this subject is planned for the near future.

5. Acknowledgments

We would like to acknowledge the support of Lander Ibarra and Daniel Nunez of Argonne National Laboratory for their contribution of user documentation and feedback. We would also like to like to thank Bob Reid and Katrina Sweetland of Los Alamos National Laboratory, who have provided substantial advice on heat pipe theory and assistance with interpretation of experimental data.

Table 5: Performance comparison between Sockeye's heat pipe models for the SAFE-30 test problem. All times are in units of seconds. For the LCVF column, values in parentheses correspond to values when no condenser pool is modeled, where the value differs from the base case.

Parameter	**Conduction**	**LCVF**	**Two-Phase**
Evaporator elements	86	86	86
Condenser elements	154	154	154
Radial vapor elements	3	N/A	N/A
Radial wick elements	6	6	N/A
Radial cladding elements	3	3	3
Radial fuel elements	3	3	3
Total elements	3,138	2,658	1,218
Nonlinear system size	3,481	3,479	2,992
Simulation time range	0-22,000	0-22,000	7,500-7,715
Time steps	2,200	2,221(2,200)	1,044
Time step size reductions	0	24(0)	520
Average time step size	10.00	9.91(10.00)	0.21
Wall time	1,117.4	1,920.6(1,832.9)	4,692.3
Simulation time/wall time	19.68	11.45(12.00)	0.05

This work was funded by the Office of Nuclear Energy of the U.S. Department of Energy, through the Nuclear Energy Advanced Modeling and Simulation Program, under contract number DE-NE0008983. Sockeye development is being carried out under the auspices of Idaho National Laboratory, a contractor of the U.S. Government under contract number DEAC07-05ID14517. Accordingly, the U.S. Government retains a nonexclusive, royalty-free license to publish or reproduce the published form of this contribution, or allows others to do so, for U.S. Government purposes.

References

[1] D. A. Reay, P. A. Kew, R. J. McGlen, Heat Pipes: Theory, Design and Applications, sixth Edition, Elsevier Ltd., 2014.

[2] A. Faghri, Heat Pipe Science and Technology, 2nd Edition, Global Digital Press, 2016.

[3] C. Mueller, P. Tsvetkov, A review of heat-pipe modeling and simulation approaches in nuclear systems design and analysis, Annals of Nuclear Energy 160 (2021) 108393. doi:https://doi.org/10.1016/j.anucene.2021.108393.
URL `https://www.sciencedirect.com/science/article/pii/S0306454921002693`

[4] Westinghouse eVinci™ Heat Pipe Micro Reactor Technology Development, International Conference on Nuclear Engineering.

arXiv:https://asmedigitalcollection.asme.org/ICONE/proceedings-pdf/ICONE28/85246/V001T04A018/6774921/v001t04a018-icone28-67519.pdf, doi:10.1115/ICONE28-67519.
URL `https://doi.org/10.1115/ICONE28-67519`

[5] A. Faghri, C. Harley, Transient lumped heat pipe analyses, Heat Recovery Systems and CHP 14 (4) (1994) 351–363.

[6] R. S. Reid, Heat pipe transient response approximation, in: AIP Conference Proceedings, Vol. 608, American Institute of Physics, 2002, pp. 156–162.

[7] Y. Zhou, J. Wang, Z. Guo, Y. He, Y. Zhang, S. Qiu, G. Su, M. L. Corradini, 3d-2d coupling multi-dimension simulation for the heat pipe micro-reactor by moose and sam, Progress in Nuclear Energy 138 (2021) 103790. doi:https://doi.org/10.1016/j.pnucene.2021.103790.
URL `https://www.sciencedirect.com/science/article/pii/S0149197021001578`

[8] J. Hansel, L. Charlot, Sockeye heat pipe analysis code verification and validation, in: The 19th International Topical Meeting on Nuclear Reactor Thermal Hydraulics (NURETH-19), Brussels, Belgium, 2022.

[9] M. L. Hall, J. M. Doster, A sensitivity study of the effects of evaporation/condensation accommodation coefficients on transient heat pipe modeling, International Journal of Heat and Mass Transfer 33 (3) (1990) 465–481.

[10] J.-M. Tournier, M. El-Genk, A heat pipe transient analysis model, International Journal of Heat and Mass Transfer 37 (5) (1994) 753–762.

[11] V. H. Ransom, H. Chow, Athena heat pipe transient model, Space Nuclear Power Systems (1987) 389–392.

[12] J. E. Hansel, R. A. Berry, D. Andrs, M. S. Kunick, R. C. Martineau, Sockeye: A one-dimensional, two-phase, compressible flow heat pipe application, Nuclear Technology 207 (7) (2021) 1096–1117. arXiv:https://doi.org/10.1080/00295450.2020.1861879, doi:10.1080/00295450.2020.1861879.
URL `https://doi.org/10.1080/00295450.2020.1861879`

[13] A. D. Lindsay, D. R. Gaston, C. J. Permann, J. M. Miller, D. Andrš, A. E. Slaughter, F. Kong, J. Hansel, R. W. Carlsen, C. Icenhour, L. Harbour, G. L. Giudicelli, R. H. Stogner, P. German, J. Badger, S. Biswas, L. Chapuis, C. Green, J. Hales, T. Hu, W. Jiang, Y. S. Jung, C. Matthews, Y. Miao, A. Novak, J. W. Peterson, Z. M. Prince, A. Rovinelli, S. Schunert, D. Schwen, B. W. Spencer, S. Veeraraghavan, A. Recuero, D. Yushu, Y. Wang, A. Wilkins, C. Wong, 2.0 - MOOSE: Enabling massively parallel multiphysics simulation, SoftwareX 20 (2022) 101202. doi:https://doi.org/10.1016/j.softx.2022.101202.
URL `https://www.sciencedirect.com/science/article/pii/S2352711022001200`

[14] R. Martineau, D. Andrs, R. Carlsen, D. Gaston, J. Hansel, F. Kong, A. Lindsay, C. Permann, A. Slaughter, E. Merzari, R. Hu, A. Novak, R. Slaybaugh, Multiphysics for nuclear energy applications using a cohesive computational framework, Nuclear Engineering and Design 367 (2020) 110751. doi:https://doi.org/10.1016/j.nucengdes.2020.110751.
URL `https://www.sciencedirect.com/science/article/pii/S0029549320302454`

[15] Y. Wang, S. Schunert, J. Ortensi, V. Laboure, M. DeHart, Z. Prince, F. Kong, J. Harter, P. Balestra, F. Gleicher, Rattlesnake: A MOOSE-based multiphysics multischeme radiation transport application, Nuclear Technology 207 (7) (2021) 1047–1072. doi:10.1080/00295450.2020.1843348.
URL `https://doi.org/10.1080/00295450.2020.1843348`

[16] Z. M. Prince, J. T. Hanophy, V. M. Labouré, Y. Wang, L. H. Harbour, N. Choi, Neutron transport methods for multiphysics heterogeneous reactor core simulation in Griffin, Annals of Nuclear Energy 200 (2024) 110365. doi:https://doi.org/10.1016/j.anucene.2024.110365.
URL `https://www.sciencedirect.com/science/article/pii/S0306454924000276`

[17] R. L. Williamson, J. D. Hales, S. R. Novascone, G. Pastore, K. A. Gamble, B. W. Spencer, W. Jiang, S. A. Pitts, A. Casagranda, D. Schwen, A. X. Zabriskie, A. Toptan, R. Gardner, C. Matthews, W. Liu, H. Chen, BISON: A flexible code for advanced simulation of the performance of multiple nuclear fuel forms, Nuclear Technology 207 (7) (2021) 954–980. doi:10.1080/00295450.2020.1836940.
URL `https://doi.org/10.1080/00295450.2020.1836940`

[18] C. Matthews, V. Laboure, M. DeHart, J. Hansel, D. Andrs, Y. Wang, J. Ortensi, R. C. Martineau, Coupled multiphysics simulations of heat pipe microreactors using DireWolf, Nuclear Technology 207 (7) (2021) 1142–1162. doi:10.1080/00295450.2021.1906474.
URL `https://doi.org/10.1080/00295450.2021.1906474`

[19] J. Hansel, D. Andrs, L. Charlot, G. Giudicelli, The MOOSE thermal hydraulics module, Journal of Open Source Software 9 (94) (2024) 6146. doi:10.21105/joss.06146.
URL `https://doi.org/10.21105/joss.06146`

[20] J. Hansel, J. Hartvigsen, L. Ibarra, P. Sabharwall, B. Feng, Sockeye validation support using the sphere facility, in: International Conference on Physics of Reactors 2022 (PHYSOR 2022), 2022.

[21] E. Toro, Riemann Solvers and Numerical Methods for Fluid Dynamics: A Practical Introduction, Springer Berlin Heidelberg, 2009.

[22] R. A. Berry, R. Saurel, O. LeMetayer, The discrete equation method (DEM) for fully compressible, two-phase flows in ducts of spatially varying cross-section, Nuclear Engineering and Design 240 (2010) 3797–3818.

[23] A. Chinnayya, E. Daniel, R. Saurel, Modelling detonation waves in heterogeneous energetic materials, Journal of Computational Physics 196 (2004) 490–538.

[24] V. Carey, Liquid-Vapor Phase-Change Phenomena: An Introduction to the Thermophysics of Vaporization and Condensation Processes in Heat Transfer Equipment, 3rd Edition, CRC Press, 2020. doi:https://doi.org/10.1201/9780429082221.

[25] F. M. White, H. Xue, Fluid Mechanics, ninth Edition, McGraw-Hill, New York, NY, 2021.

[26] C. F. Curtiss, J. O. Hirschfelder, Integration of stiff equations*, Proceedings of the National Academy of Sciences 38 (3) (1952) 235–243. arXiv:https://www.pnas.org/doi/pdf/10.1073/pnas.38.3.235, doi:10.1073/pnas.38.3.235.
URL `https://www.pnas.org/doi/abs/10.1073/pnas.38.3.235`

[27] T. Cotter, Theory of heat pipes, Tech. Rep. LA-3246-MS, Los Alamos National Laboratory (1965).

[28] C. A. Busse, Pressure drop in the vapor phase of long heat pipes, in: Proceedings of IEEE Conference of Thermionic Conversion Specialists, Palo Alto, CA, 1967, pp. 391–398.

[29] J. W. L. Paul F. Fischer, S. G. Kerkemeier, nek5000 Web page, http://nek5000.mcs.anl.gov (2008).

[30] D. Shaver, A. Obabko, A. Tomboulides, J. Fang, H. Yuan, Y. Yu, S. Tutwiler, D. Dai, N. Saini, C. Boyd, Nek5000: improvements in the available rans models, meshing, tutorials, and training, Tech. rep., Argonne National Lab. (ANL), Argonne, IL (United States) (2021).

[31] M. N. Ivanovskii, V. P. Sorokin, I. V. Yagodkin, The Physical Principles of Heat Pipes, Oxford University Press, 1982.

[32] M. El-Genk, J.-M. Tournier, Uses of liquid-metal and water heat pipes in space reactor power systems, Frontiers in Heat Pipes (FHP) 2 (1) (2011).

[33] M. V. Dyke, J. Martin, M. Houts, Overview of non-nuclear testing of the safe, affordable 30-kw fission engine, including end-to-end demonstrator testing, Tech. Rep. NASA/TM-2003-212930 (2003).

[34] R. S. Reid, J. T. Sena, A. L. Martinez, Sodium heat pipe module test for the SAFE-30 reactor prototype, in: AIP Conference Proceedings, Vol. 552, 2001, pp. 869–874.